

Exact Mass Conservation in Binary Neutron Star Merger Simulations

Boris Daszuta¹, Sebastiano Bernuzzi¹, Joan Fontbuté¹, Ruocheng Zhai^{2,4}, Alan Tsz-Lok Lam^{2,3}, Jacob Fields⁵, and David Radice^{2,3,4}

¹*Theoretisch-Physikalisches Institut, Friedrich-Schiller-Universität Jena, 07743, Jena, Germany*

²*Institute for Gravitation and the Cosmos, The Pennsylvania State University, University Park PA 16802, USA*

³*Department of Physics, The Pennsylvania State University, University Park PA 16802, USA*

⁴*Department of Astronomy & Astrophysics, The Pennsylvania State University, University Park PA 16802, USA and*

⁵*Institute for Advanced Study, Princeton, NJ 08540, USA*

(Dated: June 1, 2026)

A long-standing problem in the simulation of neutron star spacetimes is the treatment of vacuum regions outside the stars. The use of an artificial low-density atmosphere is a common robust approach within Eulerian hydrodynamics that, however, introduces baryon-mass violation even with conservative numerical schemes. We propose a simple numerical algorithm that ensures exact mass conservation by means of an appropriate local rescaling of the atmosphere. The scheme is combined with a low-order flux correction and it can be further augmented by a pseudo-vacuum treatment that enforces strict vacuum in the outer regions far from the central objects. We demonstrate the effectiveness of these vacuum treatments with binary neutron star merger simulations spanning multiple orbits and the postmerger phase, and including a microphysical equation of state. The rescaling algorithm guarantees mass and electron number conservation to round-off precision. The pseudo-vacuum treatment shows slightly larger but approximately constant violations and can improve the computation of fast tail ejecta as well as provide convergent gravitational waves of quality comparable to the standard atmosphere. Overall, results from different atmosphere treatments and a two-code comparison suggest that current computations of gravitational waves and (dynamical) ejecta in the presence of an artificial atmosphere are robust, provided that conservative adaptive mesh refinement with flux correction is employed.

I. INTRODUCTION

The simulation of neutron star spacetimes requires handling vacuum regions and the dynamical transition between vacuum and fluid on the computational domain, see e.g. discussions in [1–5]. For example, the exterior spacetime of a compact star is vacuum and needs to be included in the computational domain. Vacuum encompasses the spatial regions distant from the strong-field regime of a binary neutron star merger (BNSM), where gravitational waves (GWs) are extracted. Matter ejecta unbound during the merger dynamics expand and fill these vacuum regions along the evolution. Vacuum regions can also appear after black hole formation as matter flows in and accretes onto the black hole. The treatment of vacuum regions is a central practical issue to obtain successful numerical-relativity simulations of astrophysical interest.

The most common approach to neutron star simulations is conservative Eulerian hydrodynamics with high-resolution shock capturing schemes. In this context, it is standard practice to substitute vacuum with a dilute atmosphere and let the numerical scheme handle sharp gradients at the matter-vacuum interface. While robust solutions are available, this procedure introduces artifacts. Baryon (rest) mass violation is commonly observed even when finite volume (FV) schemes and conservative adaptive mesh refinement (AMR) techniques are employed. This violation may, in principle, impact the accurate computation of mass ejecta and gravitational waves and introduce a slowly (if at all) converging systematic error

in the computations. Similarly, sound waves, velocity gradients up to $\sim 0.6c$ and temperature gradients up to a few MeV can develop at matter-vacuum interfaces in BNSM altering the thermodynamical state of the simulated matter, e.g. [6, 7], and potentially affecting microphysics (ejecta composition, weak-reaction rates, etc).

In Newtonian hydrodynamics the matter-vacuum transition can be handled by specific Riemann solvers and/or level set methods [8, 9]. However, this approach significantly complicates the algorithms, especially with non-trivial grid geometries or AMR. This is even more serious in presence of gravity, where the treatment of vacuum regions can alter hydrostatic equilibria between the fluid's pressure and the gravity pull. Specific well-balanced numerical schemes have been introduced to exactly preserve hydrostatic equilibrium solutions, and were found essential to simulate astrophysical fluids, e.g. [10–12] and references therein.

In general-relativistic hydrodynamics, numerical issues are amplified by the errors introduced during the numerical inversion of conservative to primitive variables. Such transformation is (typically) not analytical and failures during the inversion (even floating-point drift) handled via flooring can cause violation of mass conservation. Non-conservative AMR treatment is another cause of mass conservation violation [13–15].

While these are very well known problems for practitioners, no rigorous and robust alternative exists so far and the use of an artificial atmosphere is the most common approach in neutron stars simulations. A vacuum treatment has been proposed in Poudel *et al.* [16] (see also [17]) indicating some advantages for neutron

star simulations with the BAM code [4, 18]. However, the method still violates mass conservation. More recently, the first-order flux correction (FOFC) approach of Lemaster and Stone [19] has been applied to BNSM simulations with AthenaK [20, 21]. The method significantly reduced mass violation and appears to improve simulation robustness.

In this paper, we explore a new numerical algorithm to ensure exact mass conservation in neutron star space-time simulations. The scheme relies on an appropriate rescaling of the standard atmosphere treatment and can be easily incorporated in existing codes. It can be further augmented by a pseudo-vacuum treatment that enforces strict vacuum in the outer regions far from the central objects. These methods are implemented in the GR-Athena++ AMR code together with a low-order flux correction [5, 22, 23].

The paper is organized as follows. Section II introduces the details of the rescaling algorithm, of the low-order flux correction and the pseudo-vacuum treatment. Section III presents first results for BNSM simulations with a focus on mass ejecta and GWs. A direct comparison with AthenaK is also discussed. Conclusions are in Sec. IV

II. METHOD

We focus on the (3+1)D balance-law formulation of Eulerian general-relativistic hydrodynamics (GRHD) [24]. The local conservation law for the Eulerian mass-density ¹,

$$\partial_t \tilde{D} + \partial_i F_D^{(i)} = 0 \quad (1)$$

where $F_{\tilde{D}}$ is the appropriate flux, guarantees baryon (rest) mass conservation,

$$M_b = \int_{\Sigma_t} d^3x \tilde{D}, \quad \dot{M}_b(t) = 0, \quad (2)$$

if the integral is taken on the entire 3D spatial hypersurface Σ_t . When the fluid composition is incorporated in the equation of state (EOS), as common, hydrodynamics equations are augmented by conservation or balance laws for particle species. For example, the number of electrons per baryons (nucleons) Q_e is conserved according to the local conservation law for the electron fraction Y_e ,

$$\partial_t(\tilde{D}Y_e) + \partial_i F_{Y_e}^{(i)} = 0. \quad (3)$$

If neutrino radiation is simulated (outside the scope of this paper), Y_e evolves based on weak-interaction rates introduced as source terms at the r.h.s. of Eq. (3).

Conservative FV methods are designed precisely to preserve these continuum properties at the discrete level. Nonetheless during numerical computations, the values of M_b and Q_e can (and usually do) drift beyond what can be ascribed to outflow through the computational domain. The origin of the violation is usually the treatment of vacuum region and the use of non-conservative AMR. Note that violations are not limited to floating-point errors but are often due to failures during primitive reconstruction, in particular if the variable inversion is handled with flooring [5, 6].

A. Standard atmosphere

A standard approach to deal with vacuum regions is to adjust the initial data through the introduction of an unphysical, static atmosphere, over each cell where the matter density is zero. The atmosphere points are then evolved in the same way as the other fluid cells. Atmosphere floors may be applied at various steps of the evolution in order to avoid division by zero and prevent the evolution towards unphysical states. A common choice is to enforce atmosphere floors during the conservative to primitive variable inversion. Here, a fluid cell that has evolved below atmosphere level is reset to a floor value. In case the numerical inversion fails, a point may also be reset to the atmosphere floors.

The choice of floor values is implementation dependent and based on experimentation with hydrostatic problems, e.g. spherical neutron stars spacetimes. The specific implementation adopted in GR-Athena++ and considered for our work is described in [5, 6] and available open source ². For a composition-dependent equation of state (EOS), usually supplied in tabular form, the atmosphere at a point is fixed by imposing mass-density and temperature floors, and setting Y_e to a prescribed (atmosphere) value,

$$(D_{\text{fl}}, T_{\text{fl}}, Y_{e, \text{atm}}).$$

The choice of density and temperature floors is based on the minimum tabulated value. In atmosphere, zero fluid velocity is assumed and all the other quantities are computed consistently with the EOS.

B. Rescaling

As a remedy to drifts in M_b and Q_e we propose a simple rescaling procedure of the atmosphere that keeps under control the violation in conserved quantities. At any timestep we compute the violation in conservation based on the difference between current and initial value,

¹ Tilde always indicates densitization by the spatial 3-metric γ_{ij} ; i.e. $\tilde{D} = \sqrt{\det \gamma} D$. Einstein's index-summation convention is understood with $i = 1, 2, 3$.

² <https://computationalrelativity.github.io/grathenacode/>

$\delta M_b(t) = M_b(t) - M_b(0)$ (and similarly for Q_e .) After a timestep, the violation is then driven to zero, $\delta M_b \rightarrow 0$, by rescaling the atmosphere over regions containing matter at near-atmosphere levels. To achieve this we proceed with an iterative prescription.

We define the ‘‘cutoff integral’’

$$\mathcal{I}[D; f_D] := \int_{D < f_D \min(\tilde{D})} d^3x \tilde{D}, \quad (4)$$

where the parameter $f_D > 1$ serves the role of controlling the upper bound for data that will be rescaled. For a chosen cutoff f_D we iteratively set $f_D \leftarrow f_D^2$ until $\mathcal{I}(D; f_D) > \delta M_b$ is satisfied³. Finally, at all points such that $D \leq f_D \min(D)$ the mass density is rescaled by

$$\tilde{D} \leftarrow \tilde{D} \times \frac{M_b(0) - \mathcal{I}[D; f_D]}{M_b(t) - \mathcal{I}[D; f_D]}. \quad (5)$$

The overall procedure is terminated if the mass (or Q_e) violation deviates excessively from its initially recorded value. This is determined by monitoring the absolute relative error of the corresponding conserved quantity with respect to its initial value. A threshold of 10^{-4} was chosen to disable rescaling for all salient runs. We stress that the rescaling assumes no outflow from the computational domain and absence of sources or sinks in the domain of integration.

The rescaling we have described may be combined with standard atmosphere treatments. It may also be used in conjunction with the approach described in Sec. II C which we term pseudo-vacuum.

C. Pseudo-vacuum

One alternative to global imposition of atmosphere is to only introduce floors in regions local to matter. Prior to evaluation of a time-integrator stage, cells with $D > 0$ are flagged as ‘‘matter containing’’. Floors are then only imposed on the remaining cells if any nearest-neighbour⁴ cell contains matter. This introduces a thin layer of atmosphere. The time sub-step is then calculated for the flagged cells, with the layer providing support for flux computations. After a full time-step, any cell whose density falls below a prescribed cutoff D_{cut} is reset to strict vacuum; no rescaling is imposed during sub-steps.

Applying the above procedure, allows matter to flow into regions initially without matter, with spatial extent developing dynamically according to the simulation. In vacuum regions, the matter field evolution is thereby entirely trivialized, which also serves to reduce computational cost of the matter sector evaluation in proportion

to the relative size of the inactive region. A similar strategy is implemented in the BAM code, although we note that BAM AMR is not exactly conservative [4, 15, 16].

D. AMR implementation with Low-order Flux correction

The algorithms described above have been implemented in the GR-Athena++ code [5, 22, 23]. GR-Athena++ employs high-resolution shock-capturing (HRSC) schemes based on conservative FV methods and block-based AMR. The code has been extended with a low-order flux-correction (LOFC), further supplemented by an approximate discrete-maximum-principle (DMP) [26], as motivated by improved robustness and conservation properties observed with the first-order flux correction (FOFC) in [20, 21]. We briefly summarize the procedure below.

At each time sub-step, numerical fluxes at interfaces are assembled based on (primitive) reconstruction (here WENO5Z [27]), and combined according to the local-Lax-Friedrichs (LLF) prescription [28]. This gives rise to a candidate state vector for the conserved Eulerian variables (prior to addition of any geometric source-terms). If the candidate state does not satisfy DMP, or would require atmosphere flooring (Sec. II A), the cell is flagged for LOFC. If flagged, for all interfaces adjacent to the problem-cell, we switch to low order primitive reconstruction (here PLM-van Leer [29]), and recompute the LLF fluxes. This flux correction remains conservative, and is used to propagate the state instead. The LOFC is applied to all simulations presented below.

III. APPLICATION TO BNSM

We now compare the standard, rescaling, and pseudo-vacuum (PV) atmosphere treatments discussed in Sec. II in BNSM simulations. To this end, we consider the evolution of equal-mass quasicircular irrotational BNS data with mass $M = 2.7 M_{\odot}$; initial data are prepared based on the Lorene solver [30]. Neutron star matter is described by the temperature-dependent DD2 EOS [31]. The DD2 binary evolves for ~ 4.5 orbits and produces a long-lived remnant; the simulations are further conducted until at least 20 ms postmerger.

The computational domain is a Cartesian mesh over the volume defined by $[-2268, 2268]^3$ km with AMR setup that closely follows the cell-centered setup of Daszuta *et al.* [23]. The domain is sampled with $N_M = 96$ or 144 points in each dimension, decomposed in mesh blocks of fixed sampling 16^3 points and recursively refined (at 2 : 1 refinement-ratio) until a target, minimum resolution is achieved. The finest resolutions considered for three setups are $\delta x_c \simeq 492.2$ m, $\delta x_m \simeq 369.2$ m, and $\delta x_f \simeq 246.1$ m. No mesh symmetries are imposed. Time stepping is performed with strong-stability preserving

³ We evaluate this via a numerical quadrature and employ Kahan-Babushka-Neumaier compensated summation [25].

⁴ Our implementation leaves this freely specified; here we only consider immediate nearest-neighbours.

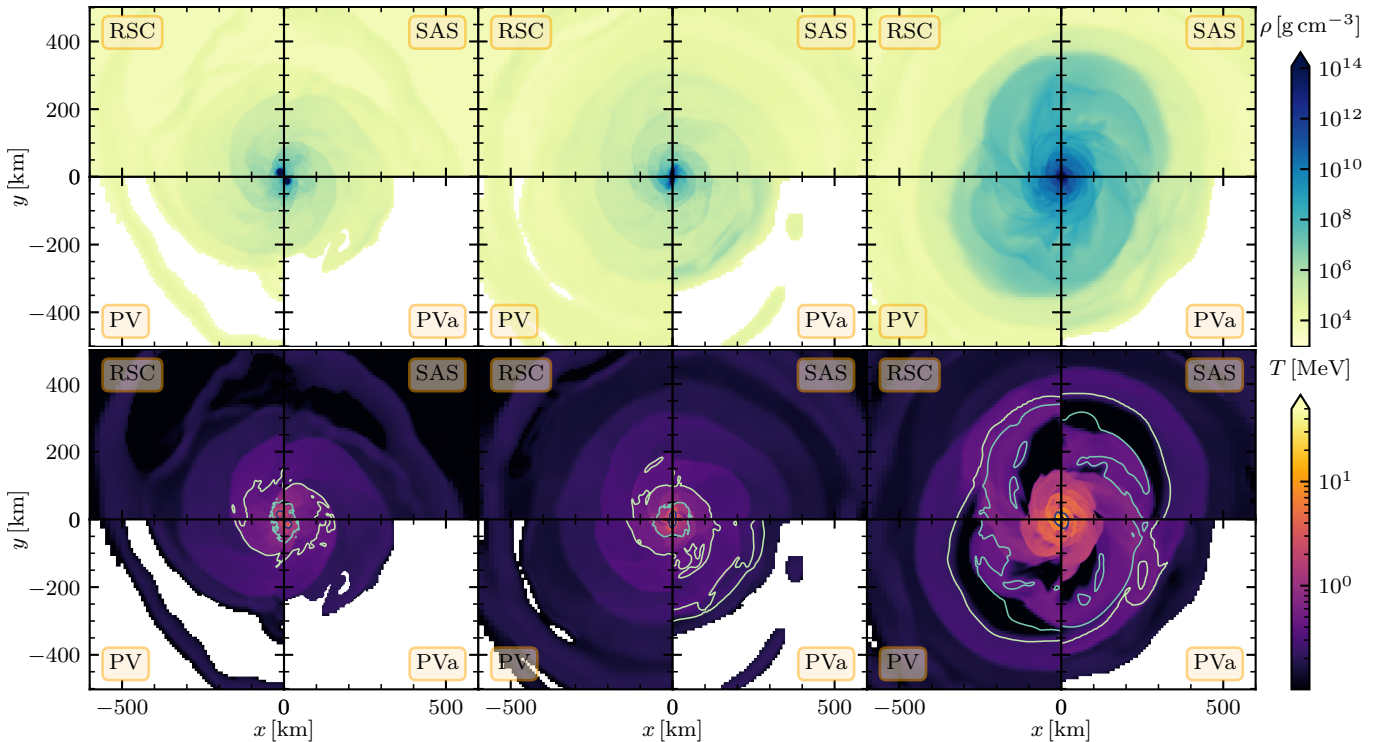


FIG. 1. Rest-mass density ρ (top) and temperature T (bottom) evolution in the orbital plane for four atmosphere treatments. Each column shows a snapshot of the remnant at fixed time where column-wise we have: $t - t_{\text{mrgr}} \simeq (-4.8, 0.4, 4.2)$ ms. At fixed time, four quadrants are displayed for ρ and T . For each variable we show in the (upper right quadrant) the standard atmosphere treatment (SAS), (upper left) rescaling, (lower left) pseudo-vacuum (PV) with $D_{\text{cut}} = 9.7 \times 10^3 \text{ g cm}^{-3}$, and (lower right) PV with more aggressive $D_{\text{cut}} = 32 \times 10^3 \text{ g cm}^{-3}$ denoted (PVa). For the T panels we additionally overlay isodensity contours at: $\rho = 10^{12} \text{ g cm}^{-3}$ (dark blue), $\rho = 10^7 \text{ g cm}^{-3}$ (pale green), and $\rho = 5 \times 10^5 \text{ g cm}^{-3}$ (pale yellow). Data depicted here correspond to simulations with grid-setup featuring finest level resolution of δx_f .

Runge-Kutta SSPRK(3,3) [32] and Courant-Friedrich-Lewy condition of 0.25 is set.

We next discuss results for simulations performed at the three common resolutions for four distinct atmosphere treatments: (i) the standard atmosphere treatment (denoted SAS), (ii) the rescaling algorithm with $f_D = 10 = f_{Y_e}$ (denoted RSC), (iii) the pseudo-vacuum algorithm with f_D and f_{Y_e} as in RSC, and cut chosen as $D_{\text{cut}} = 9.7 \times 10^3 \text{ g cm}^{-3}$ (denoted PV), and (iv) the PV algorithm with a more aggressive choice of $D_{\text{cut}} = 32 \times 10^3 \text{ g cm}^{-3}$ (denoted PVa). For all simulations, floor and atmosphere parameters are set as $(D_{\text{fl}}, T_{\text{fl}}, Y_{e, \text{atm}}) = (6 \times 10^3 \text{ g cm}^{-3}, 0.1 \text{ MeV}, 0.5)$. We emphasize that each of these four setups is otherwise identical to the others, only differing in the details of the atmosphere treatment.

A. Mass and Electron number conservation

Snapshots at distinct times of the evolution of the (fluid-frame) density together with temperature in the orbital plane for the DD2 binary are shown in Fig. 1 for the four atmosphere treatments. As is common in all BNSM simulations, matter leaks out from the star sur-

faces before merger and fills a region around the stars at densities *above* the atmosphere threshold and temperatures of a few MeV. The rescaling algorithm cannot avoid this effect, which is observed with all treatments. At merger, matter compresses and bounces while the two cores fuse to form a remnant with maximum densities $\rho_{\text{max}}^{\text{remnant}} \sim 1.3 \rho_{\text{max}}^{\text{NS}}$, where $\rho_{\text{max}}^{\text{NS}}$ is the initial maximum density of the isolated NS. Pressure waves propagating outwards steepen into shock waves with densities $\lesssim \rho_{\text{max}}^{\text{NS}}$ and peak temperatures $T \sim 70 \text{ MeV}$ [33]. These waves develop into spiral density waves [34] and rapidly fill the entire computational domain with matter densities above the atmosphere. These dynamics are observed for all atmosphere treatments with negligible quantitative difference. Notably, even the PV treatments do not alter the picture: the orbital motion and hydrodynamics flow around remnants are all consistent at densities above atmosphere.

Figure 2 shows the relative error in the baryon mass and electron number conservation. The conservative AMR and standard atmosphere treatment in GR-Athena++ guarantees relative baryon mass violations $\lesssim 10^{-6}$ at the (moderate) resolution considered for these simulations. The violation constitutes mass *gain*. For the runs presented here, with the standard atmosphere treat-

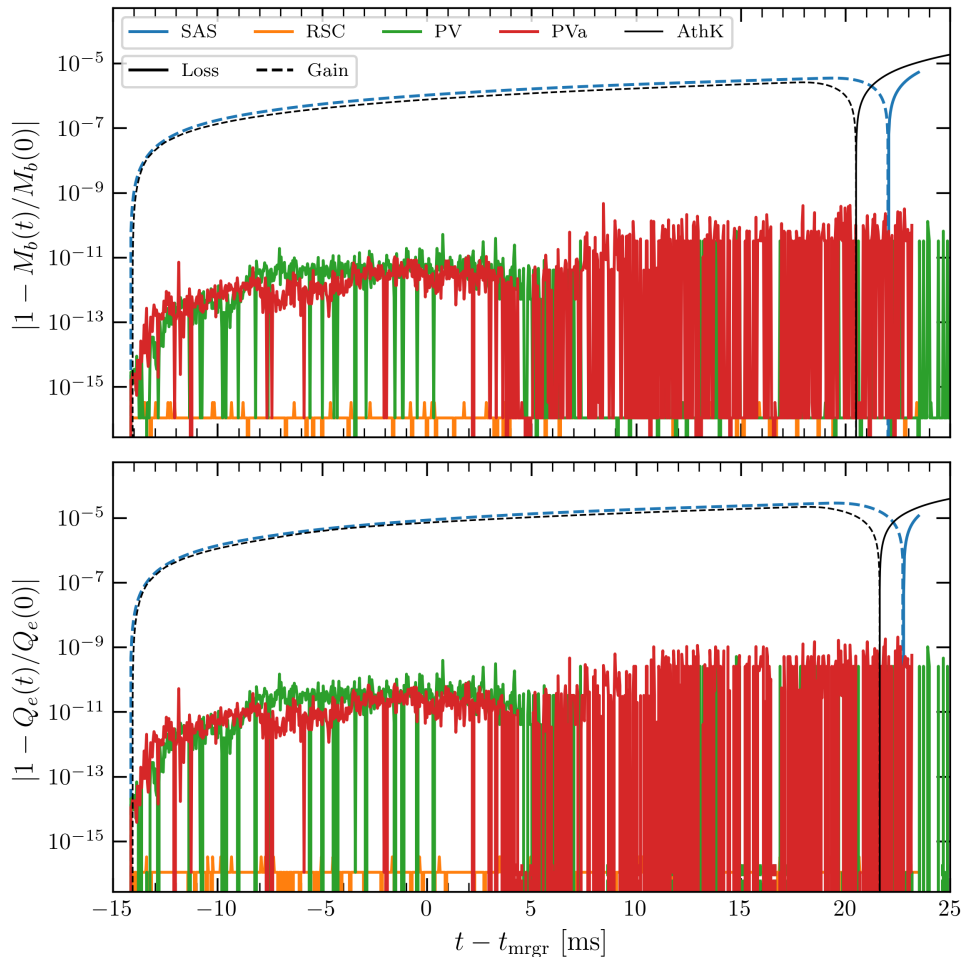


FIG. 2. Evolution of the relative error in baryon (rest) mass and electron number conservation for the four vacuum algorithms at fixed finest resolution δx_f . Dashed (solid) lines highlight mass or electron number gains (losses). The plot demonstrates exact (to round off error) conservation for both quantities with the rescaling algorithm (RSC) introduced in our work, and an approximately constant violation $\lesssim 10^{-11}$ with both variants of pseudo-vacuum (PV, PVa) algorithm. The standard atmosphere treatment (SAS) introduces relative gains of order $\sim 10^{-6}$ in both mass and electron number conservation. Simulations involving the lower resolutions δx_c and δx_m display comparable behaviour (not depicted here). **AthenaK** data obtained with a very similar simulation setup as **GR-Athena++** SAS are shown in black.

ment, this can be understood as follows. In regions exterior to the binary constituents, prior to significant generation of mass ejecta, matter is typically near-atmosphere. During the evolution, atmosphere accretes, thereby pushing D below D_H . This in turn, leads to artificial injection of matter as floors are applied. On the other hand, the rescaling algorithm delivers mass conservation to round off precision, with exterior regions falling below the dynamically inferred cut that enters the algorithm (f_D). The PV treatment shows similar mass conservation but to $\lesssim 10^{-11}$ level. This larger violation compared to the rescaling is related to the mass violation during a time integrator timestep.

The conservation of electron number is also shown in Fig. 2, bottom panel. The behaviour closely mirrors the behaviour of the mass, indicating that the largest violations in this quantity are also due to the vacuum treatment.

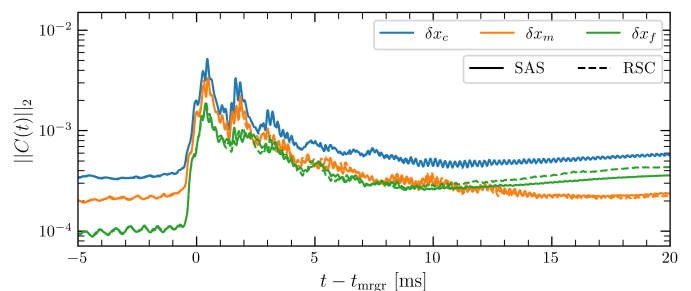


FIG. 3. Evolution of the L_2 -norm of the Z4c collective constraint monitor $C(t)$ for DD2 BNS simulations, at a variety of resolutions, and different atmosphere treatments. The standard treatment (solid lines) and the rescaled (dashed lines) atmosphere treatments are seen to agree well, for runs with grids involving finest resolutions δx_c , δx_m , and δx_f .

GR-Athena++ employs the Z4c free evolution scheme for the spacetime evolution [35, 36]. The numerical solution of free-evolution schemes introduces violation of the Einstein constraints as well as other constraints related to the specific hyperbolic formulation of Einstein field equations. It is therefore important to assess that the new vacuum treatments do not introduce further violations of such constraints.

Figure 3 shows the evolution of the L_2 norm of the collective Z4c constraint monitor C for the standard and rescaled atmosphere treatment at the three mesh resolutions. The specific expression for C includes Hamiltonian and momentum constraints as well as the four Z -constraints, see Eq. (40) of [37] for its expression. Note the calculation of the norm of the constraint monitor excludes points towards grid boundaries where approximate Sommerfeld boundary can lead to relatively large local violations (while being stable.) The constraint monitor for the two treatments are consistent with each other and converge to zero as resolution is increased. The constraint violation in these simulations is largely dominated by hydrodynamical truncation errors that are, in turn, dominated by the bulk fluid motion (i.e. not by the constant atmosphere.) The postmerger dynamics in particular is characterized by a more complex flow and shocks and therefore typically shows slower convergence. Our novel treatment does not significantly impact on constraint violations. Similar results are found for PV treatments, not shown in the figure.

B. Ejecta

During the first core bounce, part of the matter becomes unbound and generates dynamical ejecta [38]. Figure 4 shows the evolution of the ejecta mass (top) and the mass-averaged asymptotic velocity (bottom) for the lowest resolution simulations. These quantities are computed by flagging fluid elements that reach a sphere at coordinate radius $R \simeq 591$ km with outwards-pointing velocity using either the Bernoulli criterion, i.e. $hu_t < -h_{\min}$, where h and h_{\min} are the specific and minimum (of the EOS table) enthalpies, and u_t the time component of the fluid 4-velocity, or the geodesic criterion, $u_t < -1$.

At earlier times $t - t_{\text{mrgr}} < 5$ ms the mass ejection is spurious and mainly related to low density material around the stars. Here, the Bernoulli criterion significantly overestimates the ejecta, cf. [39]. The standard and rescaled atmosphere treatments behave very similarly, while the PV treatment reduces the early, spurious mass ejection since no significant mass is present at the extraction sphere. Note, however, the PV treatments can exhibit a larger velocity peak due to clumps of material propagating in the pseudo vacuum.

The bulk of the dynamical ejecta reaches the coordinate sphere at $t \sim 5$ ms postmerger. At these times the mass rises quickly by about an order of magnitude to $\sim 10^{-4} M_{\odot}$ and the averaged asymptotic velocity peaks

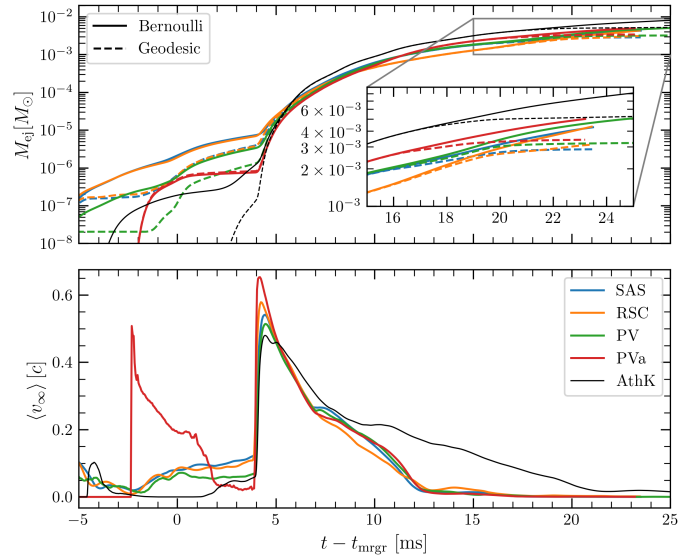


FIG. 4. Evolution of ejecta mass (top) and mass-averaged velocity (bottom) for the four atmosphere algorithms. Unbound mass is monitored either according to Bernoulli criterion (solid lines) or geodesic criterion (dashed line) and extracted at a sphere of coordinate radius $R \simeq 591$ km. Common (finest) resolution of these runs is δx_f . AthenaK data obtained with a very similar simulation setup as GR-Athena++ SAS are shown in black.

at $\sim 0.4 - 0.6 c$, independently of the atmosphere treatment. The dynamical ejecta quickly saturate afterwards to a total mass of $\sim 5 \times 10^{-3} M_{\odot}$. Their velocity rapidly decreases towards zero (more on this below). At later postmerger times $t \gtrsim 20$ ms, the dynamical ejecta terminates, and all simulations show the beginning of the early spiral-wave wind from the remnant. The latter is captured only by the Bernoulli criterion.

In order to verify that all atmosphere treatments reproduce the same ejecta, we compute the mass-weighted histograms of the angular distribution in the latitude angle ϑ with respect to the orbital plane and of the asymptotic mass-averaged velocity. These quantities are shown in Fig. 5. As expected for equal-mass mergers, the bulk ejecta is concentrated around the orbital plane with half opening angle of ~ 30 degrees. The different vacuum treatments in GR-Athena++ do not significantly alter the spatial distribution of the ejecta.

The asymptotic mass-averaged velocities also behave very similarly when different vacuum treatments are considered (bottom panel of Fig. 5.). Main differences are present in the fast tail of the ejecta. The more aggressive pseudo-vacuum treatment (PVa) can resolve fast tails with velocities up to $\lesssim 0.8c$ at the considered resolution, while standard atmosphere treatment resolves up to $\sim 0.65c$ in this simulation. Fast tails are composed of low density material just above the atmosphere level; the launch and propagation of this material is facilitated by the higher cutting value for the vacuum threshold D_{cut} in PVa.

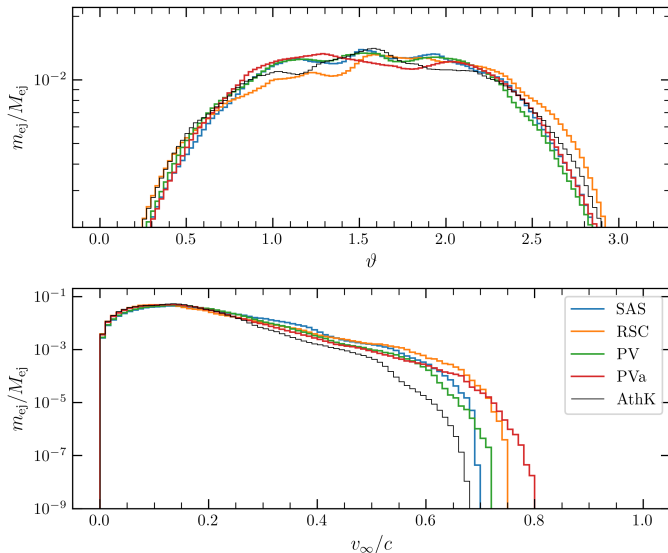


FIG. 5. Mass-weighted histograms of ejecta angular distribution (top) and asymptotic velocity (bottom). Unbound mass is monitored according to the Bernoulli criterion and extracted at a sphere of coordinate radius $R \simeq 591$ km. The cumulative histograms are computed at $t - t_{\text{mrgr}} = 21$ ms. Common (finest) resolution of these runs in δx_f . AthenaK data obtained with a very similar simulation setup as GR-Athena++ SAS are shown in black.

We remark that in the presented results the bulk of the ejecta is mostly contained on the computational grid and start to outflow at ~ 20 ms postmerger, see Fig. 2. For the simulated timescale, this does not significantly affect the rescaling algorithm. However, for significantly longer evolution it may be necessary to dynamically change the rescaling parameters according to the physical mass outflowing the domain. This does not pose major conceptual difficulties and could also be adopted for matter accreting onto (through) an apparent horizon.

C. Gravitational Waves

We next explore the computation of gravitational waves in simulations with different atmosphere treatment. Figure 6 compares the dominant mode of the strain and the instantaneous wave frequency computed with the standard atmosphere and rescaling algorithm at different resolutions. Minor differences in the wave amplitudes and phases are visible only at the highest resolution and in the postmerger part of the wave. In particular, the use of the rescaling algorithm appears to produce a slightly more compact remnant towards the end of the gravitational-wave dominated postmerger phase at these resolutions. In turn, the waveform's amplitude is slightly larger (less damped) at around $t \sim 6$ ms postmerger. Similar results are found for the pseudo-vacuum treatments.

Waveform's phase self-convergence plots are shown in

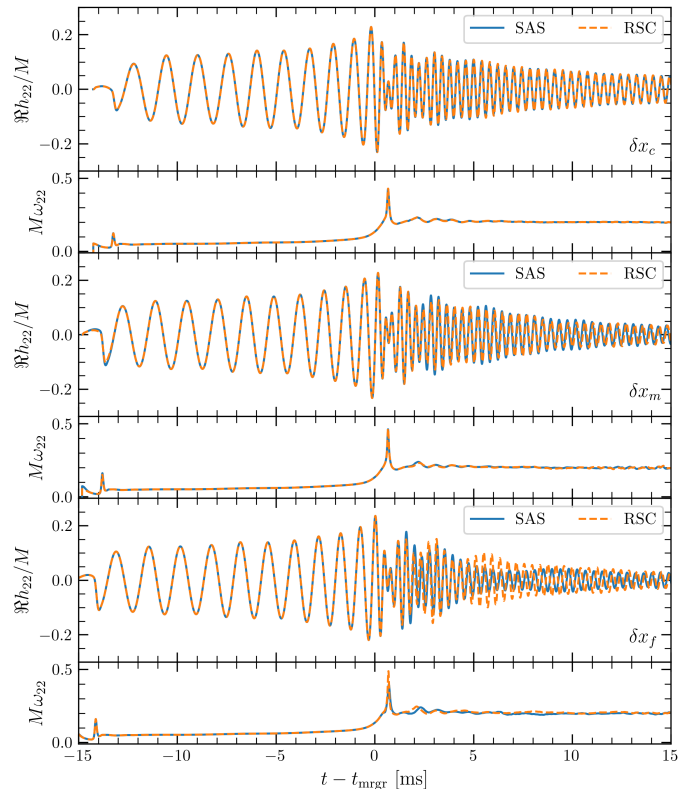


FIG. 6. Gravitational waves strain and instantaneous frequency. Real part and instantaneous frequency of the $(\ell m) = (22)$ mode of the strain, based on evolution with the standard atmosphere treatment (SAS) in (blue, solid lines), and rescaling (RSC), in (orange, dashed lines). Top, middle, and bottom panels are computed from simulations involving finest resolutions of δx_c , δx_m , and δx_f respectively. Waves are extracted at a sphere of coordinate radius $R \simeq 295.3$ km.

Fig. 7. All the atmosphere treatments give consistent second-order convergent results in the inspiral phase of the evolution. In the postmerger phase, the standard atmosphere treatment leads to second-order convergent waveforms, differently from what previously observed in [22, 23]. This we attribute to LOFC, which was not previously available. Waveform convergence progressively degrades in the postmerger phase for the RSC and PV treatments at the considered resolution. The more aggressive PVa treatment, however, does achieve approximate second-order convergence. These results indicate that the combination of atmosphere treatment and AMR flux-correction scheme are potentially key to achieve postmerger waveform convergence already at the moderate resolutions considered here.

D. Comparison with AthenaK

We finally compare the vacuum treatments in GR-Athena++ with AthenaK. The same simulations presented above have been repeated using a very simi-

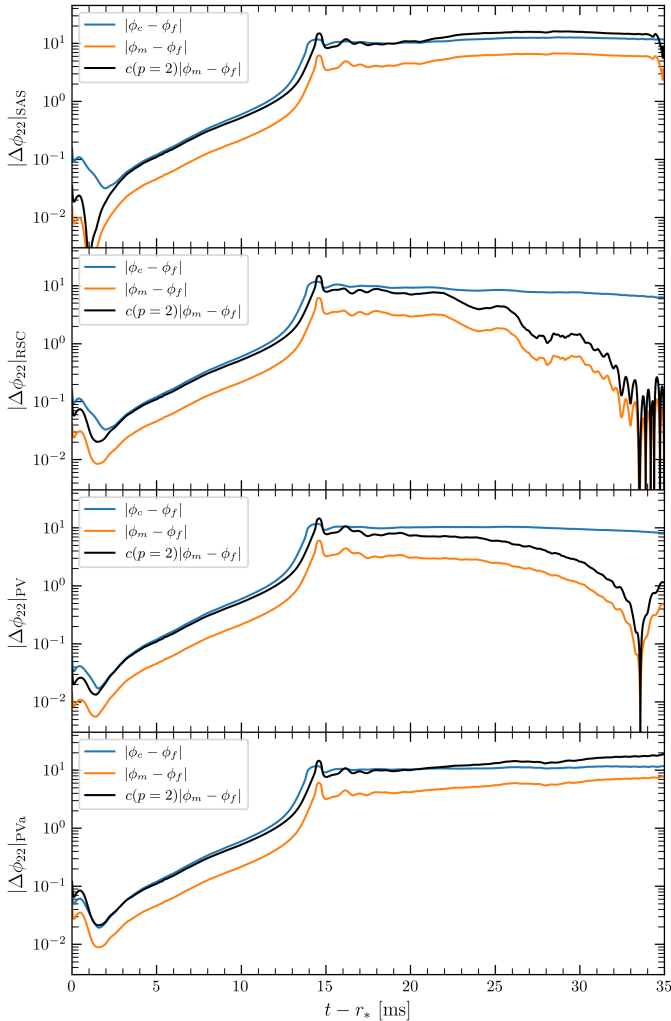


FIG. 7. Self convergence of the phase of the gravitational wave’s leading mode extracted at $R \simeq 295.3$ km for the different atmosphere treatments: SAS, RSC, PV and PVa from top to bottom respectively.

lar, although not identical setup in the *AthenaK* code. The atmosphere treatment is very similar to the one in *GR-Athena++*. However, *AthenaK* conservative AMR implements a different flux-correction: the FOFC described in [19–21]. The grid setup closely mirrors the *GR-Athena++* setup, but the AMR criterion is slightly different [21]. In particular, the resolution at the wave (ejecta) extraction sphere of *AthenaK* is $\sim 3.94, 5.91, 3.94$ km ($\sim 7.88, 11.81, 7.88$ km) for the three resolutions, while in *GR-Athena++* is $\sim 7.88, 5.91, 7.88$ km ($\sim 15.75, 11.81, 15.75$ km). Outflows are computed using a latitude-longitude grid on the extraction sphere with $N_\theta = 256$, $N_\phi = 512$ points and coordinate radius $R \simeq 591$ km. Both codes extract GWs on geodesic grids at the extraction spheres (*GR-Athena++* uses 9002 vertices and *AthenaK* 1002) by computing the Weyl pseudoscalar ψ_4 and integrating via fixed frequency integration (FFI) [40].

The violation of baryon mass and lepton number conservation with the standard atmosphere treatments in *GR-Athena++* and *AthenaK* is shown in Fig. 2. Despite implementation differences in the AMR and flux-correction the performances of the two codes are very comparable. While performing this comparison, we discovered an issue with scalar conservation in *AthenaK*, which produced violations at the 10^{-3} level. These emerged because Y_e could become smaller than the minimum value allowed by the EOS and would be floored. To improve mass conservation, we have augmented the FOFC scheme with a positivity preserving limiter, following the approach in [41]. Figure 2 shows the results obtained after having implemented this fix.

Ejecta properties are contrasted in Fig. 4 and Fig. 5. *AthenaK* simulation shows sustained ejecta velocity after ~ 10 ms postmerger while, as mentioned above, *GR-Athena++* ejecta velocity goes more rapidly to zero. This is due to the different structures of the AMR Cartesian grid, which results in a coarser *GR-Athena++* grid towards and at the extraction spheres of approximately a factor 2. As the low density ejecta propagate outwards they are practically absorbed into the atmosphere or the vacuum. At the same time, the comparison confirms that the RSC and PV treatments help to better resolve the fast tail of the bulk of dynamical ejecta (see above).

Regarding the gravitational waveforms, Fig. 8 shows the phase and amplitude (relative) differences of the leading mode of the signal between *AthenaK* and the four atmosphere treatments implemented in *GR-Athena++* at the highest considered resolution δx_f . During the inspiral, the phase differences are consistently lower than 0.1 rad (and flat) while amplitude relative differences are below 1%. These differences are comparable to (or smaller than) truncation errors at the considered resolution. As anticipated by Fig. 6, differences are more prominent in the postmerger phase. *AthenaK* data are closer to the *GR-Athena++* RSC and PV treatments. Larger differences are found with SAS and PVa at later times, which however achieve convergence at the considered resolutions (cf. Fig. 7). We note that, while the AMR criterion in *AthenaK* guarantees higher resolution at the extraction spheres than in *GR-Athena++*, it does not generate a grid hierarchy that is suitable for a consistent three-level convergence test in the wave zone.

IV. CONCLUSION

In this paper, we proposed a simple yet efficient algorithm to ensure exact mass conservation in Eulerian general-relativistic simulations of neutron star spacetimes. In its simplest form, the scheme is a dynamical rescaling of the low-density atmosphere floors that can be easily incorporated in existing codes. Such a rescaling can be coupled with a pseudo-vacuum treatment that enforces strict vacuum in exterior regions and reduces simulation cost proportionally to the extent of the latter.

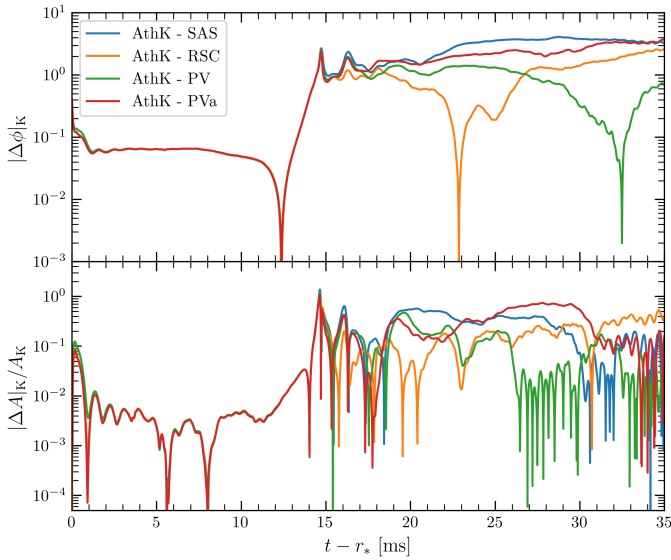


FIG. 8. Gravitational waves phase (top) and amplitude (bottom) differences of the four atmosphere treatments (SAS-blue, RSC-orange, PV-green and PVa-red) implemented in **GR-Athena++** with respect to **AthenaK** data. Waves are extracted at a sphere of coordinate radius $R \simeq 295.3$ km. Simulations are at resolution δx_f .

We demonstrated the effectiveness of these vacuum treatments with BNSM simulations spanning multiple orbits and the GW-driven postmerger phase, and including a microphysical equation of state. The comparison of gravitational waves and (dynamical) ejecta computed with different atmosphere treatments indicates that these observables are only very mildly affected by the vacuum treatment and are therefore robust. The comparison between **GR-Athena++** and **AthenaK** clearly highlights that implementation details matter. Moreover we found crucial the use of conservative AMR with flux corrections for achieving robust conservation of baryonic mass (and more broadly, other extant conserved charges).

The proposed rescaling and pseudo-vacuum treatment may be relevant in long-term evolutions of BNSM, also in the presence of neutrino radiation. Improved mass conservation and pseudo-vacuum treatment can improve the accuracy of mass-outflow computation when typical densities reach value comparable to the density floors. Such simulations may require monitoring mass outflowing from the computational domain and dynamically correcting the algorithmic parameters, $(M_b(0), f_D)$ in Eq. (5). A similar adjustment could be required in presence of black hole formation, in order to improve the remnant disc evolution.

The proposed scheme also allows exact electron number conservation in absence of neutrino radiation. In

presence of the latter, the scheme should be adjusted taking into account the source terms in the electron fraction balance law. Ultimately, the scheme may lead to an improved lepton number conservation. Analogously to the dynamical mass adjustment discussed above, there is no immediate difficulty incorporating these changes but extensive experimentation is likely needed. These explorations are ongoing.

ACKNOWLEDGMENTS

BD, JF and SB acknowledge support by the EU Horizon under ERC Consolidator Grant, no. InspiReM-101043372. DR acknowledges support from the U.S. Department of Energy, Office of Science, Division of Nuclear Physics under Award Number(s) DE-SC0021177 and DE-SC0024388; and from the National Science Foundation under Grants No. PHY-2020275, PHY-2116686, PHY-2407681, and PHY-2512802. DR and JMF acknowledge support from NASA under Award Number 80NSSC25K7213.

GR-Athena++ simulations were performed on the national HPE Apollo Hawk (Hunter) at the High Performance Computing Center Stuttgart (HLRS). The authors acknowledge HLRS for funding this project by providing access to the supercomputer HPE Apollo Hawk (Hunter) under the grant numbers INTRHYGUE/44215 and MAGNETIST/44288. Simulations were also performed on SuperMUC_NG at the Leibniz-Rechenzentrum (LRZ) Munich. The authors acknowledge the Gauss Centre for Supercomputing e.V. (www.gauss-centre.eu) for funding this project by providing computing time on the GCS Supercomputer SuperMUC-NG at LRZ (allocations `pn67xo`, `pn761i`, `pn68wi` and `pn36jo`). The authors gratefully acknowledge the computing time provided on the high-performance computer Lichtenberg II at TU Darmstadt, funded by the German Federal Ministry of Research, Technology and Space (BMFTR), and the State of Hesse Ministry of Science and Research, Art and Culture (HMWK). **AthenaK** simulations were performed on Aurora at the Argonne Leadership Computing Facility, which is a DOE Office of Science User Facility supported under Contract DE-AC02-06CH11357. An award of computer time was provided by the INCITE program. **AthenaK** simulations were also performed on Perlmutter, at the National Energy Research Scientific Computing Center (NERSC), a Department of Energy User Facility, using NERSC award ERCAP0031370. Postprocessing and development runs were performed on the ARA cluster at Friedrich Schiller University Jena. The ARA cluster is funded in part by DFG grants INST 275/334-1 FUGG and INST 275/363-1 FUGG, and ERC Starting Grant, grant agreement no. BinGraSp-714626.

[1] J. A. Font *et al.*, Phys. Rev. **D65**, 084024 (2002), arXiv:gr-qc/0110047.

[2] H. Dimmelmeier, J. A. Font, and E. Müller, Astron.

- Astrophys. **388**, 917 (2002), arXiv:astro-ph/0204288.
- [3] L. Baiotti, I. Hawke, P. J. Montero, F. Loffler, L. Rezzolla, *et al.*, Phys.Rev. **D71**, 024035 (2005), arXiv:gr-qc/0403029 [gr-qc].
- [4] M. Thierfelder, S. Bernuzzi, and B. Brügmann, Phys.Rev. **D84**, 044012 (2011), arXiv:1104.4751 [gr-qc].
- [5] W. Cook, B. Daszuta, J. Fields, P. Hammond, S. Albanesi, F. Zappa, S. Bernuzzi, and D. Radice, Astrophys. J. Suppl. **277**, 3 (2025), arXiv:2311.04989 [gr-qc].
- [6] W. Kastaun, J. V. Kalinani, and R. Ciolfi, Phys. Rev. D **103**, 023018 (2021), arXiv:2005.01821 [gr-qc].
- [7] P. Hammond, I. Hawke, and N. Andersson, Phys. Rev. D **104**, 103006 (2021), arXiv:2108.08649 [astro-ph.HE].
- [8] E. F. Toro, *Riemann Solvers and Numerical Methods for Fluid Dynamics*, 2nd ed. (Springer-Verlag, 1999).
- [9] R. J. LeVeque, *Finite Volume Methods for Hyperbolic Problems* (Cambridge University Press, 2002).
- [10] P. Chandrashekar and C. Klingenberg, SIAM Journal on Scientific Computing **37**, B382 (2015), <https://doi.org/10.1137/140984373>.
- [11] J. P. Berberich, R. Käppeli, P. Chandrashekar, and C. Klingenberg, arXiv e-prints, arXiv:2005.01811 (2020), arXiv:2005.01811 [math.NA].
- [12] P. V. F. Edelmann, L. Horst, J. P. Berberich, R. Andrassy, J. Higl, G. Leidi, C. Klingenberg, and F. K. Röpke, Astron. and Astrophys. **652**, A53 (2021), arXiv:2102.13111 [astro-ph.SR].
- [13] W. E. East, F. Pretorius, and B. C. Stephens, Phys.Rev. **D85**, 124010 (2012), arXiv:1112.3094 [gr-qc].
- [14] C. Reisswig, R. Haas, C. D. Ott, E. Abdikamalov, P. Mösta, D. Pollney, and E. Schnetter, Phys. Rev. **D87**, 064023 (2013), arXiv:1212.1191 [astro-ph.HE].
- [15] T. Dietrich, S. Bernuzzi, M. Ujevic, and B. Brügmann, Phys. Rev. **D91**, 124041 (2015), arXiv:1504.01266 [gr-qc].
- [16] A. Poudel, W. Tichy, B. Brügmann, and T. Dietrich, Phys. Rev. D **102**, 104014 (2020), arXiv:2009.06617 [gr-qc].
- [17] W. Tichy, L. Ji, A. Adhikari, A. Rashti, and M. Pirog, Class. Quant. Grav. **40**, 025004 (2023), arXiv:2212.06340 [gr-qc].
- [18] B. Brügmann, J. A. Gonzalez, M. Hannam, S. Husa, U. Sperhake, *et al.*, Phys.Rev. **D77**, 024027 (2008), arXiv:gr-qc/0610128 [gr-qc].
- [19] M. N. Lemaster and J. M. Stone, Astrophys. J. **691**, 1092 (2009), arXiv:0809.4005 [astro-ph].
- [20] J. M. Stone, P. D. Mullen, D. Fielding, P. Grete, M. Guo, P. Kempfski, E. R. Most, C. J. White, and G. N. Wong, arXiv e-prints, arXiv:2409.16053 (2024), arXiv:2409.16053 [astro-ph.IM].
- [21] J. Fields, H. Zhu, D. Radice, J. M. Stone, W. Cook, S. Bernuzzi, and B. Daszuta, Astrophys. J. Suppl. **276**, 35 (2025), arXiv:2409.10384 [astro-ph.HE].
- [22] B. Daszuta and W. Cook, “GR-Athena++: Magnetohydrodynamical Evolution with Dynamical Space-Time,” (2025) arXiv:2406.05126 [gr-qc].
- [23] B. Daszuta, W. Cook, P. Hammond, J. Fields, E. M. Gutiérrez, S. Bernuzzi, and D. Radice, Phys. Rev. D **112**, 103006 (2025), arXiv:2406.09139 [gr-qc].
- [24] F. Banyuls, J. A. Font, J. M. A. Ibanez, J. M. A. Martí, and J. A. Miralles, Astrophys. J. **476**, 221 (1997).
- [25] A. Neumaier, ZAMM - Journal of Applied Mathematics and Mechanics / Zeitschrift für Angewandte Mathematik und Mechanik **54**, 39 (1974), <https://onlinelibrary.wiley.com/doi/pdf/10.1002/zamm.1974054039>.
- [26] B. Daszuta, S. Bernuzzi, M. Jacobi, E. M. Gutiérrez, P. Hammond, W. Cook, and D. Radice, (2026), arXiv:2602.18290 [gr-qc].
- [27] R. Borges, M. Carmona, B. Costa, and W. S. Don, Journal of Computational Physics **227**, 3191 (2008).
- [28] L. D. Zanna and N. Bucciantini, Astron. Astrophys. **390**, 1177 (2002), arXiv:astro-ph/0205290.
- [29] B. van Leer, Journal of Computational Physics **14**, 361 (1974).
- [30] E.ourgoulhon, P. Grandclement, K. Taniguchi, J.-A. Marck, and S. Bonazzola, Phys.Rev. **D63**, 064029 (2001), arXiv:gr-qc/0007028 [gr-qc].
- [31] M. Hempel, T. Fischer, J. Schaffner-Bielich, and M. Liebendorfer, Astrophys. J. **748**, 70 (2012), arXiv:1108.0848 [astro-ph.HE].
- [32] S. Gottlieb and C.-W. Ketcheson, David I. and Shu, Journal of Scientific Computing **38**, 251 (2009).
- [33] A. Perego, S. Bernuzzi, and D. Radice, Eur. Phys. J. **A55**, 124 (2019), arXiv:1903.07898 [gr-qc].
- [34] V. Nedora, S. Bernuzzi, D. Radice, A. Perego, A. Endrizzi, and N. Ortiz, Astrophys. J. **886**, L30 (2019), arXiv:1907.04872 [astro-ph.HE].
- [35] S. Bernuzzi and D. Hilditch, Phys. Rev. **D81**, 084003 (2010), arXiv:0912.2920 [gr-qc].
- [36] D. Hilditch, S. Bernuzzi, M. Thierfelder, Z. Cao, W. Tichy, and B. Brügmann, Phys. Rev. **D88**, 084057 (2013), arXiv:1212.2901 [gr-qc].
- [37] A. Weyhausen, S. Bernuzzi, and D. Hilditch, Phys. Rev. **D85**, 024038 (2012), arXiv:1107.5539 [gr-qc].
- [38] D. Radice, A. Perego, K. Hotokezaka, S. A. Fromm, S. Bernuzzi, and L. F. Roberts, Astrophys. J. **869**, 130 (2018), arXiv:1809.11161 [astro-ph.HE].
- [39] W. Kastaun and F. Galeazzi, Phys.Rev. **D91**, 064027 (2015), arXiv:1411.7975 [gr-qc].
- [40] C. Reisswig and D. Pollney, Class.Quant.Grav. **28**, 195015 (2011), arXiv:1006.1632 [gr-qc].
- [41] D. Radice, L. Rezzolla, and F. Galeazzi, Class.Quant.Grav. **31**, 075012 (2014), arXiv:1312.5004 [gr-qc].